POLARIZATION MODULATION FROM LENSE–THIRRING PRECESSION IN X-RAY BINARIES

Adam Ingram[1], Thomas J. Maccarone[2], Juri Poutanen[3], and Henric Krawczynski[4]

[1] Anton Pannekoek Institute, University of Amsterdam, Science Park 904, 1098 XH Amsterdam, The Netherlands; a.r.ingram@uva.nl
[2] Department of Physics, Texas Tech University, Box 41051, Lubbock, TX 79409-1051, USA
[3] Tuorla Observatory, Department of Physics and Astronomy, University of Turku, Väisäläntie 20, FI-21500 Piikkiö, Finland
[4] Physics Department and McDonnell Center for the Space Sciences, Washington University in St. Louis, 1 Brookings Drive, CB 1105, St. Louis, MO 63130, USA

ABSTRACT

It has long been recognized that quasi-periodic oscillations (QPOs) in the X-ray light curves of accreting black hole and neutron star binaries have the potential to be powerful diagnostics of strong field gravity. However, this potential cannot be fulfilled without a working theoretical model, which has remained elusive. Perhaps, the most promising model associates the QPO with Lense–Thirring precession of the inner accretion flow, with the changes in viewing angle and Doppler boosting modulating the flux over the course of a precession cycle. Here, we consider the polarization signature of a precessing inner accretion flow. We use simple assumptions about the Comptonization process generating the emitted spectrum and take all relativistic effects into account, parallel transporting polarization vectors toward the observer along null geodesics in the Kerr metric. We find that both the degree of linear polarization and the polarization angle should be modulated on the QPO frequency. We calculate the predicted absolute rms variability amplitude of the polarization degree and angle for a specific model geometry. We find that it should be possible to detect these modulations for a reasonable fraction of parameter space with a future X-ray polarimeter such as NASA's *Polarization Spectroscopic Telescope Array* (the satellite incarnation of the balloon experiment *X-Calibur*).

Key words: accretion, accretion disks – black hole physics – polarization – X-rays: binaries

1. INTRODUCTION

Low frequency quasi-periodic oscillations (hereafter QPOs) with frequencies ranging from $\sim 0.1 - 30$ Hz are routinely observed in the X-ray light curves of black hole (BH) and neutron star binary systems. The QPO properties correlate strongly with spectral state, which evolves from the hard power-law dominated *hard state* to the disk-blackbody dominated *soft state* on timescales of ∼months (Tananbaum et al. 1972; see van der Klis 2006; Done et al. 2007; Belloni 2010, for reviews). The QPO frequency increases as the spectrum softens and the amplitude rises to a peak in the hard intermediate state (HIMS: Belloni 2010) before reducing as spectral evolution continues (e.g., Muno et al. 1999; Sobczak et al. 2000). Since the flux also peaks in this state, the HIMS is ideal for studying QPOs.

The disk-blackbody spectral component is from a geometrically thin accretion disk (Novikov & Thorne 1973, p. 343; Shakura & Sunyaev 1973) and the power-law component results from Compton up-scattering of cool seed photons by a cloud of hot electrons close to the BH (Thorne & Price 1975; Sunyaev & Truemper 1979). A fraction of these seed photons are provided by the disk, with the rest generated internally in the electron cloud via cyclo-synchrotron radiation (Ghisellini et al. 1988; Poutanen & Vurm 2009; Veledina et al. 2011b). The exact geometry of the Comptonizing cloud is still a matter of debate but a prominent interpretation is the *truncated disk model* (Ichimaru 1977; Esin et al. 1997; Poutanen et al. 1997; Done et al. 2007; Gilfanov 2010, p. 17) in which the geometrically thin disk evaporates inside a radius larger than the innermost stable circular orbit (ISCO) to form a geometrically thick, optically thin ($\tau \sim 1$) accretion flow (hereafter the inner hot flow). The spectral transitions can be explained if the truncation radius moves smoothly from

$R_o \sim 60 R_g$, where $R_g = GM/c^2$, in the hard state to $R_o = R_{ISCO}$ in the soft state.

It has long been recognized that QPOs have the potential to be powerful diagnostics of the regions close to BHs. However, this potential cannot be realized without a working model, which has long remained elusive. QPO mechanisms that have been suggested in the literature either consider particle orbits in General Relativity (GR; Stella & Vietri 1998; Wagoner et al. 2001; Schnittman et al. 2006a) or instabilities in the accretion flow (Tagger & Pellat 1999; Cabanac et al. 2010). Perhaps the most successful model for explaining the array of observational properties attributes the QPO to the effect of frame dragging. In GR, a spinning massive object twists up the surrounding space time, leading to a precession of particle orbits inclined with the BH equatorial plane. This is generally called Lense–Thirring precession after the authors who originally derived it (Lense & Thirring 1918), although their derivation was only in a weak field limit, coming well before the derivation of the Kerr metric (Kerr 1963). Stella & Vietri (1998) first suggested that the QPO results from Lense–Thirring precession, considering only the precession frequency of test masses at different radii. Schnittman et al. (2006a) considered instead a precessing ring in the accretion disk. However, frequency-resolved spectroscopy reveals that it is the Comptonized spectral component that oscillates and not the disk (Markwardt et al. 1999; Revnivtsev et al. 2001; Sobolewska & Życki 2006; Axelsson et al. 2013). Ingram et al. (2009) suggested that the entire inner flow precesses as a solid body, motivated by the General Relativistic Magneto-hydro-dynamic (GRMHD) simulations of Fragile et al. (2007). This precessing flow model naturally explains the observed QPO spectrum, predicts the correct range of frequencies for BHs (Ingram et al. 2009), has been incorporated into a full model for the power spectral properties of BHs (Ingram & Done 2011, 2012a; Ingram & van der Klis 2013; Rapisarda

et al. 2014), and has been extended to also account for the optical QPOs observed from BHs (Veledina et al. 2013; Veledina & Poutanen 2015). The model can also explain the range of QPO frequencies observed in low accretion rate neutron stars (Ingram & Done 2010), but not the 11 Hz pulsar in the globular cluster Terzan 5 (Altamirano et al. 2012).

In this paper, we consider the X-ray polarization signature from a precessing inner flow. Photons emerging from a Comptonizing slab are expected to be polarized, with the polarization degree as a function of viewing angle depending on optical depth of the slab (Chandrasekhar 1960; Rybicki & Lightman 1979, p. 393; Loskutov & Sobolev 1982; Sunyaev & Titarchuk 1985; Poutanen & Svensson 1996). Although the polarization degree is predicted to be less than ~20%, the current generation of proposed X-ray polarimetry missions should comfortably be able to detect a signal. Polarimetry promises to provide a powerful extra lever arm to interpret the X-ray signal from BHs. The predicted energy dependence of the polarization signature has been extensively explored (e.g., Stark & Connors 1977; Dovčiak et al. 2008b; Li et al. 2009; Schnittman & Krolik 2009, 2010; Krawczynski 2012). Variability of the signal is less well studied, although Lense–Thirring precession did provide an early motivation for X-ray polarimetery in the 1970s (K. Long 2015, private communication). More recently, Dovčiak et al. (2008a) and Zamaninasab et al. (2011) have considered the polarization signature of orbiting hotspots and Marin & Dovčiak (2015) considered the polarization signatures of obscuring clouds, all for the case of active galactic nuclei. In this paper, we predict a modulation in the polarization signature from bright stellar-mass BHs on a timescale of ~1 s. We use simple parameterizations for the angular dependence of emission and polarization designed to mimic the results of Sunyaev & Titarchuk (1985, hereafter ST85) for the $\tau = 1$ case. We then take GR fully into account by ray-tracing photon paths from the precessing flow geometry to the observer, assuming the Kerr metric.

In Sections 2 and 3, we outline our assumed geometry and formalism for calculating the observed polarization degree and angle as a function of QPO phase. In Section 4, we consider a specific flow geometry appropriate for the HIMS and a QPO frequency of ~1−2 Hz. We calculate the amplitude of the modulation in both polarization degree and angle for the full range of observer positions. In Section 5, we discuss the prospects of detecting this signature and suggest improvements that can be made to our modeling assumptions in the future. Throughout this paper, we express distance in units of R_g and time in units of c/R_g in order to exploit the scale invariant nature of GR. We use Einstein's summing convention with Greek indices taken to run from 0 to 3 and Roman indices taken to run from 1 to 3. We adopt the four-vector formalism with negative time entries and positive spatial entries.

2. GEOMETRY

We assume the geometry proposed by Ingram et al. (2009), following Ingram & Done (2012b) and Veledina et al. (2013, hereafter VPI13). Specifically, the BH and binary system spin axes are misaligned by some modest angle β. The outer thin disk is assumed to be in the binary plane and the flow spin axis is assumed to precess around the BH spin axis, always maintaining the same misalignment angle β. In this section, we first describe our coordinate system followed by a description of the assumed geometry of the inner flow.

Figure 1. Coordinate system used in this paper. We define right-handed Cartesian coordinate systems with z-axes aligned with the BH, flow, and binary spin axes. The BH (black) and binary (red) z-axes are misaligned by the angle β and the binary system x-axis is chosen to be in the unique plane shared by the BH and binary z-axes. The vector $\hat{o}$ represents the observer's line of sight, and the BH x-axis is chosen as the projection of this vector onto the BH equatorial plane. The flow z-axis (blue) precesses around the BH z-axis with precession angle ω, always maintaining the misalignment angle β. The flow and binary z-axes are therefore aligned when $\omega = 180°$ and misaligned by an angle 2β when $\omega = 0°$.

2.1. Coordinate System

Figure 1 illustrates the coordinate system used in this paper. As in VPI13, we assume the binary spin axis is misaligned with the BH spin axis by an angle β. We define a "binary" coordinate system in which the z-axis, $\hat{z}_b$, aligns with the binary spin axis and therefore the plane of the binary is simply the plane perpendicular to $\hat{z}_b$. We choose to align the binary system x-axis with the projection of the BH spin axis on the plane of the binary. In binary coordinates, the vector pointing from the BH to the distant observer is given by

$$\hat{o} = (\sin i \cos \Phi, \sin i \sin \Phi, \cos i), \qquad (1)$$

where i is the inclination angle and Φ is the viewer azimuth. We use these angles to define the observer's position because it is possible to measure i via dynamical methods (e.g., Orosz et al. 2004, 2011). Throughout this paper, a hat denotes a unit vector.

We assume that the flow spin axis ($\hat{z}_f$) precesses around the BH spin axis, maintaining a misalignment angle β as the precession angle ω increases. This means that the misalignment between the flow and binary spin axes varies over a precession cycle between 0 and 2β. We define a "flow" coordinate system with exactly the same relationship to the binary coordinate system as introduced in VPI13. Here, however, we will perform calculations in the Kerr metric, which is azimuthally symmetric around the BH spin axis, in contrast to the Schwarzschild metric used in VPI13 which is spherically symmetric. Consequently, our calculations are greatly simplified by defining a "BH" coordinate system with basis vectors $\hat{x}$,

$\hat{y}$, and $\hat{z}$. The z-axis aligns with the BH spin axis, allowing us to use Boyer–Lindquist coordinates, and the x-axis aligns with the projection of $\hat{o}$ onto the BH equatorial plane. In this coordinate system, the observer's line of sight (LOS) can be written as

$$\hat{o} = (\sin\theta_0, 0, \cos\theta_0), \qquad (2)$$

where

$$\cos\theta_0 = \sin i \cos\Phi \sin\beta + \cos i \cos\beta, \qquad (3)$$

is the cosine of angle between the observer's LOS and the BH spin axis. We can express the flow basis vectors in this coordinate system as

$$\hat{x}_f = \left(-\cos\beta\cos(\omega-\omega_0), -\cos\beta\sin(\omega-\omega_0), \sin\beta\right)$$
$$\hat{y}_f = \left(\sin(\omega-\omega_0), -\cos(\omega-\omega_0), 0\right)$$
$$\hat{z}_f = \left(\sin\beta\cos(\omega-\omega_0), \sin\beta\sin(\omega-\omega_0), \cos\beta\right),$$
$$\qquad (4)$$

where ω_0 is the precession angle at which the projection of $\hat{z}_f$ onto the BH equatorial plane aligns with the BH x-axis (see Figure 1). This is given by

$$\tan\omega_0 = \frac{\sin i \sin\Phi}{\sin i \cos\Phi \cos\beta - \cos i \sin\beta}. \qquad (5)$$

Note that the flow y-axis always remains in the BH equatorial plane and the flow x-axis maintains a constant misalignment with the BH equatorial plane of β. When $\omega = 0°$, the flow is maximally misaligned (2β) with the disk, and when $\omega = 180°$, the flow is aligned with the disk. Any point on the surface of the flow can then be represented in this coordinate system as

$$\boldsymbol{r} = r\left(\sin\theta_f\cos\phi_f, \sin\theta_f\sin\phi_f, \cos\theta_f\right), \qquad (6)$$

where θ_f and ϕ_f are respectively the polar and azimuthal angles defined in the flow coordinate system. The same point can alternatively be represented in terms of the BH polar and azimuthal angles

$$\boldsymbol{r} = r\left(\sin\theta\cos\phi, \sin\theta\sin\phi, \cos\theta\right). \qquad (7)$$

We present the equations to convert between these two sets of coordinates in Appendix C. We can also represent a point in terms of binary polar and azimuthal angles, θ_b and ϕ_b, respectively.

2.2. Inner Hot Flow Geometry

We assume that the inner flow is shaped like a torus described in Boyer–Lindquist coordinates by the equation:

$$T(r, \theta_f) = B - \sin\theta_f[1 - (1 - B)r/r_{\mathrm{o}}], \qquad (8)$$

where $B = [(h/r)^2 + 1]^{-1/2}$, r_{o} is the outer edge, and h/r is the scale height of the flow. Outside of the flow, $T(r, \theta_f) > 0$ and inside the flow, $T(r, \theta_f) < 0$. On the flow boundary, $T(r, \theta_f) = 0$. Figure 2 shows some example cross-sections of this shape; i.e., contours of $T = 0$. For $r \ll r_{\mathrm{o}}$, the flow has a constant opening angle, with $\sin\theta_f = B$. For larger r, $\sin\theta_f \geqslant B$ and the function curves in the shape of a tear drop. We also assume an inner radiation edge, r_i, which we set equal to the ISCO in this paper. We can use Equation (8) to assess if
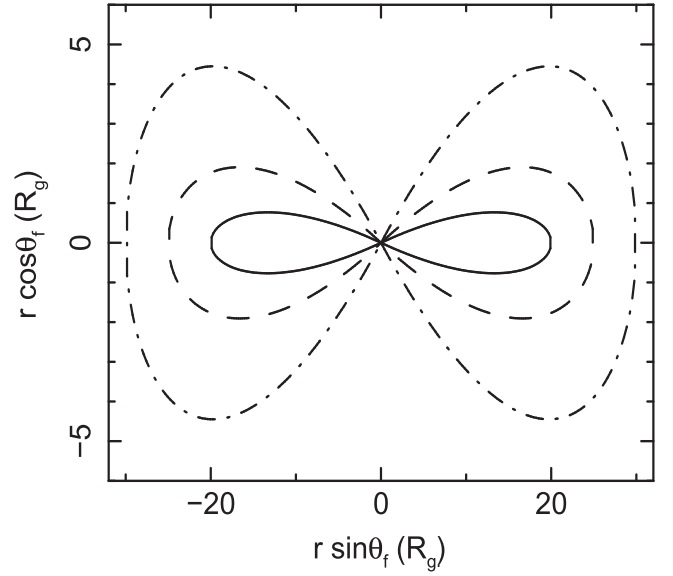
Figure 2. Illustration of the flow geometry. This depends on only two parameters: the scale height h/r and the outer radius in units of R_g, r_{o}. For $r \ll r_{\mathrm{o}}$, this function has a constant opening angle, but curves around into a tear drop shape for larger r. We show three example parameter combinations: $h/r = 0.1$, $r_{\mathrm{o}} = 20$ (solid line), $h/r = 0.2$, $r_{\mathrm{o}} = 25$ (dashed line), and $h/r = 0.4$, $r_{\mathrm{o}} = 30$ (dot–dot–dashed line). In this paper, we consider the first of these geometries, represented by the solid line.

a given position, described by the vector $\boldsymbol{r}$, is inside, outside, or on the boundary of the flow.

This shape is motivated in part by the discussion of thick disks in Chapter 10 of Frank et al. (2002). Equation (8) comes from considering an inviscid fluid rotating around a central (Newtonian) point mass (see Figure 10.2 therein). Clearly this is oversimplified, but it does provide a convenient way to parameterize the flow geometry in the most realistic way that is currently possible. Indeed, the shape illustrated in Figure 2 is comparable to those seen in GRMHD simulations (e.g., Fragile et al. 2007; Fragile & Meier 2009; Fragile 2009), which were initialized with a "Polish doughnut" solution (Jaroszynski et al. 1980) and allowed to evolve self-consistently to show solid body precession. Dexter & Fragile (2011) used "after the fact" assumptions about the radiative emissivity of the flow (following Schnittman et al. 2006b) in order to ray-trace emission from the Fragile et al. (2007) simulation but were unable to study long enough timescales to see the precession period modulate the light curve (they concentrated instead on trying to find high frequency QPO candidates). Thus defining a reasonable flow geometry analytically is currently the best way to study the effects of precession on the observed emission.

3. FORMALISM

In this section, we describe our method for calculating the flux and polarization properties observed from a precessing flow as a function of precession angle. Since we only consider linear polarization, the polarization of the signal can be described entirely by the polarization degree, p, and angle, χ.

3.1. Inner Hot Flow Properties

The specific intensity emitted from a patch of the flow surface is, in general, a function of position, photon energy, and emission angle, θ_e. Our calculations are greatly simplified by
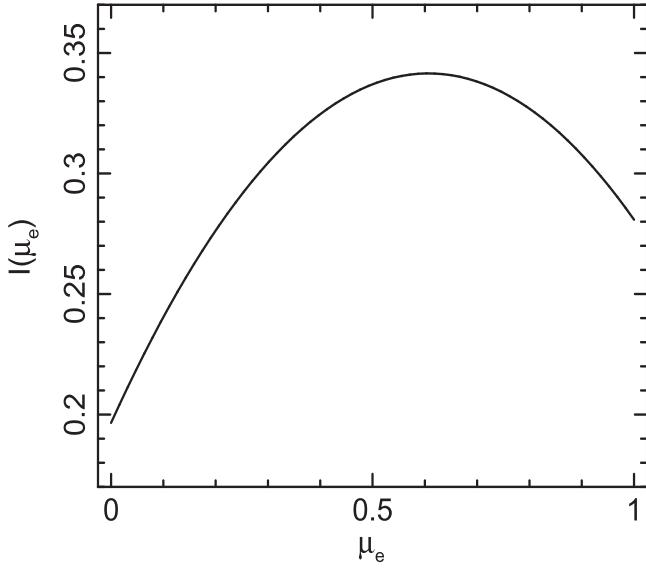
Figure 3. Intensity as a function of the emission angle assumed for this paper. We use the analytic function $I(\mu_e) \propto 1 + 1.1(1 - \mu_e) - 1.4(1 - \mu_e)^2$, designed to mimic the results of ST85 for the $\tau = 1$ case. This figure can be compared with Figure 4 of ST85, except we use a different normalization.

Figure 4. Polarization degree as a function of the emission angle assumed for this paper. We use the analytic function $p(\mu_e) = 50\%(1 - \mu_e) - 23\%[\exp\{(1 - \mu_e)^{1.6}\} - 1]$, designed to mimic the results of ST85 for the $\tau_0 = 1$ case. This figure can be compared with Figure 5 of ST85.

assuming that these variables can be separated, such that

$$I_{E_e}\left(E_e, r, \mu_e\right) = I_{E_e}\, q_e\left(r\right) I\left(\mu_e\right), \qquad (9)$$

where I_{E_e} is the emitted spectrum, $q_e(r)$ and $I(\mu_e)$ are respectively the radial and angular emissivity profiles, and $\mu_e = \cos\theta_e$. In the absence of a standard radial emissivity law for a large scale height accretion flow, we simply assume the standard case for a thin disk (Novikov & Thorne 1973, p. 343; Shakura & Sunyaev 1973)

$$q_e\left(r\right) = r^{-3}\left(1 - \sqrt{r_i/r}\right), \qquad (10)$$

following VPI13. As for the angular profile, we define an analytic function designed to mimic the shape obtained from the calculations of ST85. We plot this profile in Figure 3, to be compared with the $\tau_0 = 1$ case from Figure 4 of ST85. Here, we have normalized the intensity to give

$$2\pi \int_0^1 I(\mu_e)\mu_e d\mu_e = 1. \qquad (11)$$

We also parameterize the polarization degree as a function of emission angle $p(\mu_e)$ (defined as the fraction of photons emerging from the flow that are polarized) following the calculations of ST85. Figure 4 shows this function, and is to be compared with the $\tau_0 = 1$ case in Figure 5 of ST85. We plot $-p(\mu_e)$ in order to account for the different sign convention in ST85. We note that the emission angle θ_e is defined here with respect to the flow spin axis rather than the local normal to the torus surface. This is because the calculations of ST85 (also see Viironen & Poutanen 2004) assume Thomson scattering from a thin slab and the functions in Figures 3 and 4 are therefore only defined with respect to the flow spin axis. Since we expect the flow to have a rather small scale height ($h/r \sim 0.1$), this is likely a fairly good assumption. However, there is scope to improve upon these assumptions in future work. For instance, Poutanen & Svensson (1996) considered

cases where exact solutions can be found outside of the Thomson scattering limit.

3.2. Ray Tracing

We use the publicly available code GEOKERR, described in Dexter & Agol (2009), to solve for photon geodesics in the Kerr metric. We start off by defining an observer's camera some large distance, D, from the BH[5] along the vector $\hat{o}$. The impact parameters at infinity, α_0 and β_0, represent, respectively, the horizontal and vertical distance on the plane of the observer's camera (a schematic illustrating the impact parameters can be found to the left of Figure A1 in Middleton & Ingram 2015). For a given observer position and BH spin, a, null geodesics can be uniquely defined by these two impact parameters. Alternatively, these geodesics can be parameterized by Carter's constants of motion $l = -\alpha_0 \sin\theta_0$ and $q^2 = \beta_0^2 + \cos^2\theta_0(\alpha_0^2 - a^2)$. Each combination of impact parameters represents a pixel on the observer's camera, which is hit by a photon on a unique geodesic path. We define a grid of impact parameters with equal logarithmic steps in $b = \sqrt{\alpha_0^2 + \beta_0^2}$ and equal linear steps in the angle ϕ, defined as $\tan\varphi = \alpha_0/\beta_0$. Ignoring parallax, which is the same for each pixel, the solid angle subtended by each pixel is $b\, db d\varphi$.

For each pixel we set GEOKERR to compute 100 steps along the photon geodesic toward the BH. For each step, a position four-vector $x^\mu = (t, r, \theta, \phi)$ is provided in Boyer–Lindquist coordinates. We convert the BH polar and azimuthal angles θ and ϕ to the corresponding flow angles θ_f and ϕ_f using Equations (43) and (44). This allows us to evaluate the function $T(r, \theta_f)$ from Equation (8). If T passes from positive to negative between consecutive steps, we conclude that the geodesic has crossed the flow boundary. If this does not happen, we also check if $\mu_f \equiv \cos\theta_f$ has passed from positive

---

[5] The camera must be far enough away for all geodesics to be straight and parallel. We use $D = 10^5 R_g$.

to negative, in which case the geodesic has crossed the flow mid-plane and therefore must have crossed into *and* out of the flow in a single step. This is most likely to happen for small r where the flow is very shallow and a step does not need to be particularly large to pass completely through the flow.

In either of these cases, we have isolated a root of Equation (8) between two points on the geodesic path. We use linear interpolation to represent r as a function of μ_f between these two points, allowing us to express T as a function of μ_f only. We then find the root of the equation $T(\mu_f) = 0$ with a bisection search. From this solution for μ_f, we can interpolate a solution for r and also for ϕ_f. If $r < r_i$, we carry on following the geodesic in case it loops back around to intercept the underside of the flow. Otherwise, we calculate the contribution to the flux observed from that pixel. We ignore direct disk emission and also emission from the flow reflected from the outer disk. This assumption is appropriate for the energy range $\sim 10-20$ keV, which is dominated by Comptonized emission from the flow. Direct disk emission contributes only in soft X-rays $\lesssim 5$ keV and reflection is important at the iron line (~ 6.4 keV) and above ~ 20 keV.

3.3. Disk Shielding

When tracing rays backward from the observer, we also test whether they intercept the outer disk before hitting the flow. In this case, since the disk is optically thick, we conclude that our view of the flow is blocked for this pixel. We assume that the outer disk occupies the binary plane and truncates at $r = r_o$. At every step along the ray, we convert to binary coordinates to assess if $\mu_b \equiv \cos\theta_b$ passes from positive to negative, indicating a crossing of the disk plane. If this happens, we use linear interpolation to calculate the value of r at $\mu_b = 0$. If $r > r_o$, we conclude the ray has crossed the outer disk and stop following the ray. Otherwise, we carry on following it. In the cases where the ray crosses both the disk and flow in one step, we use linear interpolation to assess which it hit first.

3.4. Blueshift and Flux

The energy of a photon reaching the observer will be modified by the gravitational field of the BH and the motion of the emitting particle. For a stationary observer at infinity, the ratio of the observed to emitted energy of a photon (hereafter the blueshift) is given by

$$g \equiv \frac{E_o}{E_e} = \frac{-p_o^t}{p_e^\mu u_\mu}, \tag{12}$$

where p_e^μ and u^μ are respectively the four-momentum of the photon and the four-velocity of the emitting particle (e.g., Luminet 1979). We use a form for the four-momentum (given in full in Appendix A), normalized such that $p_o^t = 1$, simplifying Equation (12) further. Since we use the metric convention of negative time entries and positive distance entries, the four-velocity of the emitting particle is $(u^\mu)^2 = -(dx^\mu/ds)^2$, where $ds^2 = g_{\mu\nu}\,dx^\mu\,dx^\nu$ is the line element and $g_{\mu\nu}$ is the metric. We can represent this in terms of coordinate velocities, $\Omega^\mu \equiv dx^\mu/dt$, in the form

$$u^\sigma = \frac{\Omega^\sigma}{\sqrt{-g_{\mu\nu}\Omega^\mu\Omega^\nu}}. \tag{13}$$

We assume circular orbits ($\Omega^r = 0$) with Keplerian angular velocity about the flow spin axis, so

$$\Omega^{\phi_f} \equiv \frac{d\phi_f}{dt} = \frac{1}{r^{3/2} + a} \tag{14}$$

and $\Omega^{\theta_f} = 0$. Note, we assume Keplerian angular velocity perpendicular to the flow spin axis even for parts of the flow not in the mid-plane. Since $\Omega^{\phi_f} \gg \Omega^\omega = 2\pi\nu_{qpo}$, we convert this to BH coordinates as follows:

$$\Omega^\phi = \frac{\partial\phi}{\partial\phi_f}\Omega^{\phi_f}$$

$$\Omega^\theta = \frac{\partial\theta}{\partial\phi_f}\Omega^{\phi_f}, \tag{15}$$

where the differentials can be computed from Equations (45) and (46). We use the Kerr metric throughout, which we provide in Appendix A for completeness.

The specific flux observed at energy E_o from a pixel with solid angle $b\,db\,d\varphi$ is given by (Luminet 1979)

$$dF_{E_o} = g^3 I_{E_e}\left(E_e, r, \mu_e\right)b\,db\,d\varphi. \tag{16}$$

For energies significantly greater than the seed photon temperature (kT_{bb}) and less than the electron temperature (kT_e), the emitted spectrum can be well approximated by a power law, $I_{E_e} \propto E_e^{1-\Gamma}$. In this case, the observed spectrum is also a power law, $I_{E_o} \propto E_o^{1-\Gamma}$. Substituting this (and Equation (9)) into Equation (16), we can represent the flux in a power-law dominated energy band ($\sim 10-20$ keV) as

$$dF = g^{2+\Gamma}I_{E_o}q_e\left(r\right)I\left(\mu_e\right)b\,db\,d\varphi. \tag{17}$$

The emission angle is given by (e.g., Misner et al. 1973; Rybicki & Bromley 1997; Dovciak 2004)

$$\mu_e = g\,p_e^\mu n_\mu, \tag{18}$$

where n^μ is a four-vector normal to the flow mid-plane, defined in the flow rest frame. See Appendix B for the full form of this four-vector. The above formula encapsulates the effects of both light bending and relativistic aberration. From this, we evaluate dF for every pixel and sum to obtain the total observed flux, F, as a function of precession angle, ω.

3.5. Polarization

For each geodesic that intercepts the flow, we calculate the polarization degree from the function shown in Figure 4. We initialize the polarization four-vector, f^μ, as the projection of n^μ on the plane perpendicular to the emergent photon's four-momentum, p^μ. Following Dovciak (2004), this is defined as

$$f^\mu = \frac{n^\mu - \mu_e\left(g p_e^\mu - u^\mu\right)}{\sqrt{1 - \mu_e^2}}. \tag{19}$$

For each geodesic, we parallel transport the polarization four-vector forward from the emission point to the observer's camera in geodesic steps, δx_μ. That is, moving from s to $s + \delta s$ changes the polarization four-vector to

$$f^\mu(s + \delta s) = f^\mu(s) - f^\sigma(s)\Gamma^\mu_{\sigma\nu}\delta x^\nu, \tag{20}$$

with the Christoffel symbols given by

$$\Gamma^{\sigma}_{\mu\nu} = \frac{1}{2}g^{\sigma\kappa}\left(\frac{\partial g_{\nu\kappa}}{\partial x^{\mu}} + \frac{\partial g_{\kappa\mu}}{\partial x^{\nu}} - \frac{\partial g_{\mu\nu}}{\partial x^{\kappa}}\right). \qquad (21)$$

The position four-vector, x^{μ}, is specified for each point on each geodesic by GEOKERR, so we can simply calculate the step length as $\delta x^{\mu} = x^{\mu}(s + \delta s) - x^{\mu}(s)$.

Once we have transported f^{μ} all the way back to the observer, we convert back to BH Cartesian coordinates (see Appendix C) and find the projection of f^{μ} on the horizontal and vertical directions of the camera. These directions are given in BH (Cartesian) coordinates by

$$\hat{\boldsymbol{\alpha}}_0 = (0, 1, 0)$$
$$\hat{\boldsymbol{\beta}}_0 = (-\cos\theta_0, 0, \sin\theta_0), \qquad (22)$$

and the projections are simply $\hat{\boldsymbol{f}} \cdot \hat{\boldsymbol{\alpha}}_0$ and $\hat{\boldsymbol{f}} \cdot \hat{\boldsymbol{\beta}}_0$, where $\hat{\boldsymbol{f}}$ is the three-vector describing the spatial part of f^{μ}. The polarization angle for a given geodesic is then given by

$$\tan[\chi(\alpha_o, \beta_0)] = -\frac{\hat{\boldsymbol{f}} \cdot \hat{\boldsymbol{\alpha}}_0}{\hat{\boldsymbol{f}} \cdot \hat{\boldsymbol{\beta}}_0}. \qquad (23)$$

We define Stokes parameters for each geodesic

$$dQ = dF(\alpha_o, \beta_0)\, p(\alpha_o, \beta_0)\, \cos[2\chi(\alpha_o, \beta_0)] \qquad (24)$$
$$dU = dF(\alpha_o, \beta_0)\, p(\alpha_o, \beta_0)\, \sin[2\chi(\alpha_o, \beta_0)], \qquad (25)$$

and sum over all geodesic paths to get the observed Stokes parameters $Q = \int dQ$ and $U = \int dU$. Note that, under this convention, vertical and horizontal polarization correspond to $Q/F = 1$ and $Q/F = -1$ respectively for a 100% polarized signal. The overall polarization degree is then

$$p = \frac{\sqrt{Q^2 + U^2}}{F} \qquad (26)$$

and the overall polarization angle, χ, can be calculated from

$$\tan(2\chi) = \frac{U}{Q}. \qquad (27)$$

3.6. Simple Newtonian Approximation

In addition to the fully relativistic treatment described above, we also define a simple Newtonian approximation to assess the importance of GR effects. We make the simplifying assumption that the flow is a flat disk, so any point on the flow surface is described by the vector $\boldsymbol{r} = x\hat{\boldsymbol{x}}_f + y\hat{\boldsymbol{y}}_f$. In a flat metric, photons emitted from $\boldsymbol{r}$ hit the observer's camera at the coordinates $\alpha_0 = \boldsymbol{r} \cdot \hat{\boldsymbol{\alpha}}_0$ and $\beta_0 = \boldsymbol{r} \cdot \hat{\boldsymbol{\beta}}_0$. The Keplerian velocity (in units of c) has a magnitude $v = r^{-1/2}$ and a direction $\hat{\boldsymbol{v}} = (-y\hat{\boldsymbol{x}}_f + x\hat{\boldsymbol{y}}_f)\big/\sqrt{x^2 + y^2}$. We use Equation (17) to calculate the flux for each pixel of the camera. Using the Minkowski metric instead of the Kerr metric for Equations (13) and (12), the blueshift becomes

$$\mathsf{g} = \frac{\sqrt{1 - v^2}}{1 - \hat{\boldsymbol{o}} \cdot \boldsymbol{v}}. \qquad (28)$$

This is the special relativistic Doppler factor. Since all the photons emitted at a given time now have the same polarization angle, the observed polarization vector $\hat{\boldsymbol{f}}$ can be calculated as

the projection of $\hat{\boldsymbol{z}}_f$ onto the plane perpendicular to $\hat{\boldsymbol{o}}$ (if relativistic aberration is ignored). For the polarization angle this gives

$$\tan\chi = -\frac{\sin\beta\,\sin(\omega - \omega_0)}{\sin\theta_0\cos\beta - \cos\theta_0\sin\beta\cos(\omega - \omega_0)}, \qquad (29)$$

which is the standard formula for a rotating vector (Ferguson 1973, 1976; Viironen & Poutanen 2004). Moreover, the observed polarization degree simply becomes a flux-weighted average of the contribution from each pixel.

4. RESULTS

In our model, the geometry of the flow is governed by three parameters: the inner radius r_i, the outer radius r_o, and the scale height h/r. In this paper, we consider parameters appropriate for the HIMS and so fix $r_o = 20$ and $h/r = 0.1$ (e.g., Ingram & Done 2011, 2012a). We set $r_i = r_{\rm ISCO}$ and assume $a = 0.98$. This assumption of high spin maximizes the impact of relativistic effects, which tend to wash out variability, therefore yielding conservative estimates for the QPO amplitudes predicted by the model. This corresponds to a QPO frequency of ~ 2 Hz, typical of the HIMS. We additionally fix the misalignment angle to $\beta = 10°$ following VPI13 and assume a spectral index of $\Gamma = 2$, again typical of the HIMS.

4.1. High and Low Inclination Examples

We consider the observational appearance of the specific geometrical setup described above for a range of viewing angles. Since our geometry is asymmetric, the viewer must be specified by both a polar angle i and an azimuthal angle Φ. In this section, we first explore two specific examples, chosen to represent, respectively, high and low inclination sources. For the high inclination model, we use $i = 70°$ and $\Phi = 110°$. For the low inclination model, we use $i = 30°$ and $\Phi = 180°$. We then move on to explore a grid of viewing angles in the following subsection. For these specific examples, we use a high resolution with 400 steps in the impact parameters b and ϕ (i.e., 400×400 pixels) and we consider 32 precession angles.

Figure 5 shows images of the flow for three values of the precession angle. The right-hand images depict flux, with colors defined in arbitrary units by the key beneath. We see the characteristic apparent warping of the flow through light bending, with the back of the flow appearing to bend toward us. Since the BH is spinning rapidly, we also see an asymmetry to this apparent warping from the frame dragging effect. In the top and bottom plots, we see the underside of the flow due to rays bending dramatically from their starting points before passing through the gap between the flow and the disk and toward the observer. In reality, we may expect material in some transition region between the two accretion regimes to block our view of this secondary image to some extent. In these images, precession and rotation are anti-clockwise. We see that the brightest patch of the flow is always just to the left of the BH. This region not only has the largest radial emissivity, but emission from here is Doppler-boosted by the rapid rotation of material in the flow. Also, parts of the flow are blocked from view by the outer disk. This can be seen for all three precession angles but is perhaps clearest in the top plot where the bottom left corner of the flow is hidden behind a disk that is not pictured.
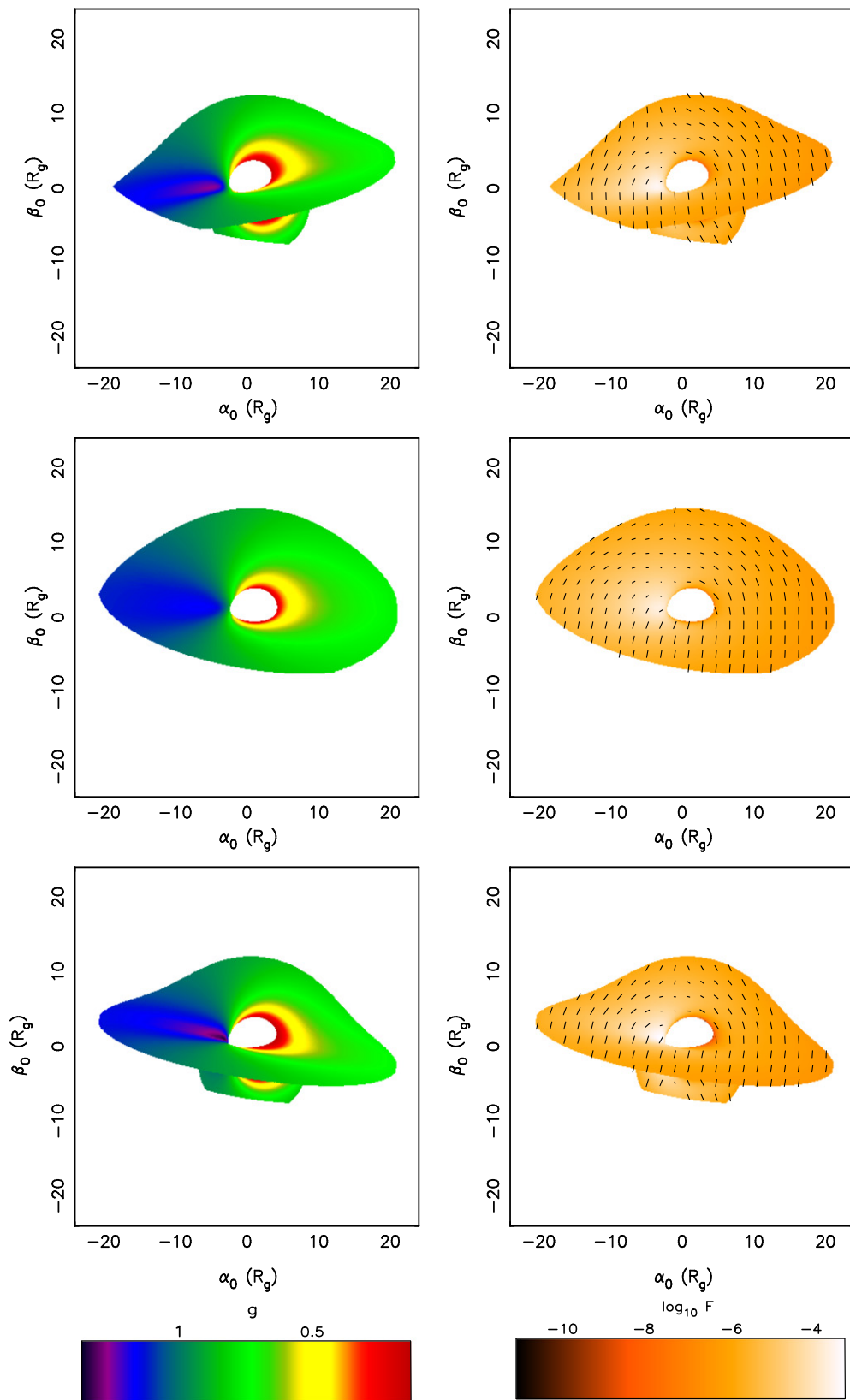
Figure 5. Images of the flow for three precession angles for the model with $i = 70°$, $\Phi = 110°$, $\beta = 10°$, and $h/r = 0.1$. The left side shows blueshift and the right side shows flux with the polarization vector overlaid, normalized to the maximum observed polarization degree. The three precession angles pictured, in units of cycles, are $\omega = 0$, 0.3125, and 0.625, from top to bottom, respectively. The full movies for these images can be found at http://figshare.com/articles/Polarization_modulation_gifs/1351920. Individual movies can alternatively be found on YouTube: www.youtube.com/watch?v=Q2CwOGKVC9U&feature=youtu.be (blueshift) and www.youtube.com/watch?v=E3kYAnS3pQI&feature=youtu.be (flux and polarization).

The images on the left show blueshift for the same three precession angles, with a key again included beneath. Emission from the approaching material to the left of the BH is blueshifted by Doppler effects, whereas the receding material to the right of the BH is redshifted. Close to the BH, we see the effects of gravitational redshift, whereby photons lose a significant amount of energy escaping the gravitational pull of the BH. For selected pixels on the right-hand plot, we also represent the polarization vector with a black line. The length of the line gives the magnitude of the polarization degree, normalized to the maximum measured from the entire run. The orientation of these vectors is heavily influenced by GR through two main effects (Stark & Connors 1977). First, light bending means that photons reaching the observer may have had a different trajectory upon emerging from the flow and therefore the polarization vectors started off misaligned with one another. Second, the parallel transport of the polarization vector in heavily curved space time further changes the orientation. These effects are, as expected, stronger for photons that passed closer to the BH, including photons from the back of the flow that emerged from relatively large radii but needed to pass very close to the BH to reach the observer. We also see an asymmetry in this effect that is directly due to the frame dragging effect. The orientation of this vector oscillates as a function of precession angle because the orientation of the flow itself is oscillating. This is diluted by GR effects but not entirely.

Figure 6 shows the (normalized) integrated flux, polarization degree, and polarization angle plotted against QPO phase for this run of the model, with solid and dashed lines respectively representing the full calculation and the simplified Newtonian approximation. We see that relativistic effects wash out variability in the flux and the polarization signature as well as reduce the average observed polarization degree and angle. The amplitude of variability is mainly reduced through light bending, which allows us to see the back of the flow even when the angle between the flow spin axis and the LOS is large. The overall polarization degree is lower for the full calculation because the polarization vectors observed from different regions of the flow are not aligned, and therefore do not add together completely constructively as in the Newtonian approximation. GR influences the polarization angle because the polarization vectors of emergent photons appear to be bent around the BH. The vectors in Figure 5 to the left of the BH are forced clockwise and those to the right are forced anticlockwise. This is a more pronounced effect on the left-hand side of the BH because the "critical point," where only light rays that are emitted perpendicular to the flow mid-plane can reach the observer, is situated here (due to frame dragging). At this point, the observer sees the polarization vector rotate, mainly due to a special relativistic aberration (see e.g., Figure 3 in Dovčiak 2010).

For the full calculation, the flux has fractional rms's of 10.0% and 2.24% in the first and second harmonics, respectively. This is representative of QPOs in high inclination sources (e.g., GRS 1915+105; Yan et al. 2013) for the first harmonic, but the amplitude of the second harmonic is slightly lower than is typically observed. For the polarization signature, we instead consider the *absolute* rms, since this is relevant for detection. These are respectively 1.0% and 0.3% for the first and second harmonics of the polarization degree and respectively $3°0$ and $0°2$ for the first and second harmonics of the polarization angle. Also, the polarization degree lags the
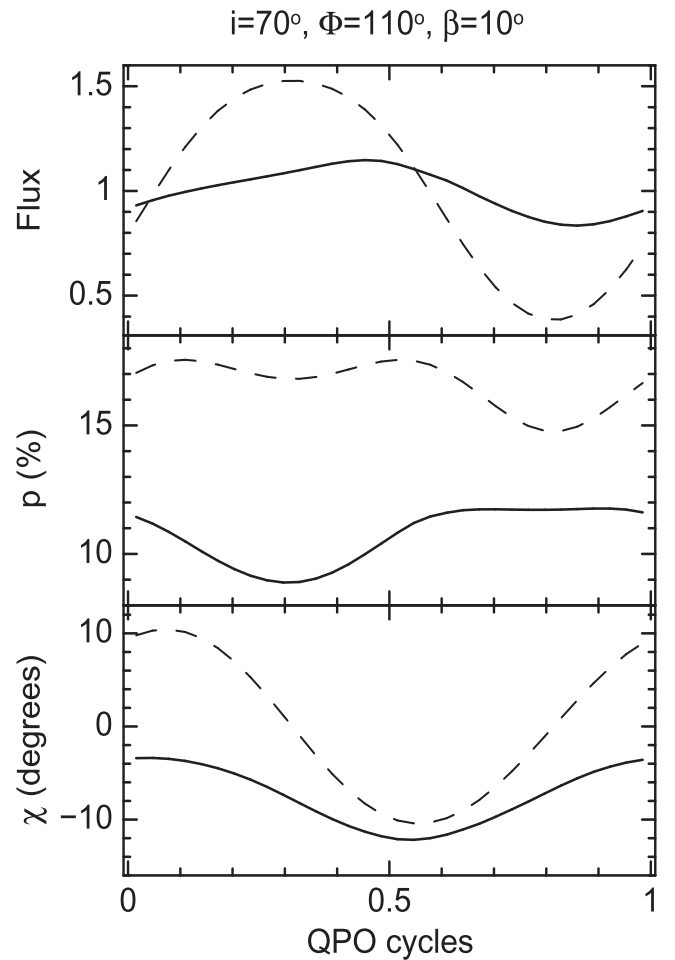
Figure 6. Flux, polarization degree, and polarization angle plotted against QPO phase for the high inclination model. The solid lines are for the fully relativistic model, and dashed lines representing a simple Newtonian approximation are included for comparison. The fractional rms's (for the full model) in the first and second harmonics, respectively, are 10.0% and 2.24% for the flux. The *absolute* rms' in the first and second harmonics are, respectively, 1.0% and 0.3% for the polarization degree, and respectively $3°1$ and $0°2$ for the polarization angle.

flux by $147°3$ for the first harmonic but the polarization angle leads the flux by $125°4$. To estimate the importance of the secondary image, we additionally perform a calculation whereby rays that pass under the disk plane and hit the underside of the flow are assumed to be blocked. For this alternative calculation, the flux has slightly higher fractional rms's of 13.3% and 3.75% for the first and second harmonics, respectively. This is because the secondary image appears to have a roughly constant shape to the observer and serves to wash out variability. The polarization properties are remarkably similar for the alternative calculation: the polarization degree has rms's of 1.0% and 0.3% for the first two harmonics and the angle has rms's of $3°1$ and $0°1$.

Figure 7 shows images of the low inclination model for the same three precession angles as previously depicted in Figure 5. For both the flux (right) and blueshift (left), we still see Doppler shifts due to rapid rotation, gravitational redshift, and the effects of light bending; however, all these effects are less pronounced since the component of velocity in the LOS is lower and also fewer photons need to pass close to the BH in order to reach the observer. The full animations for all of the
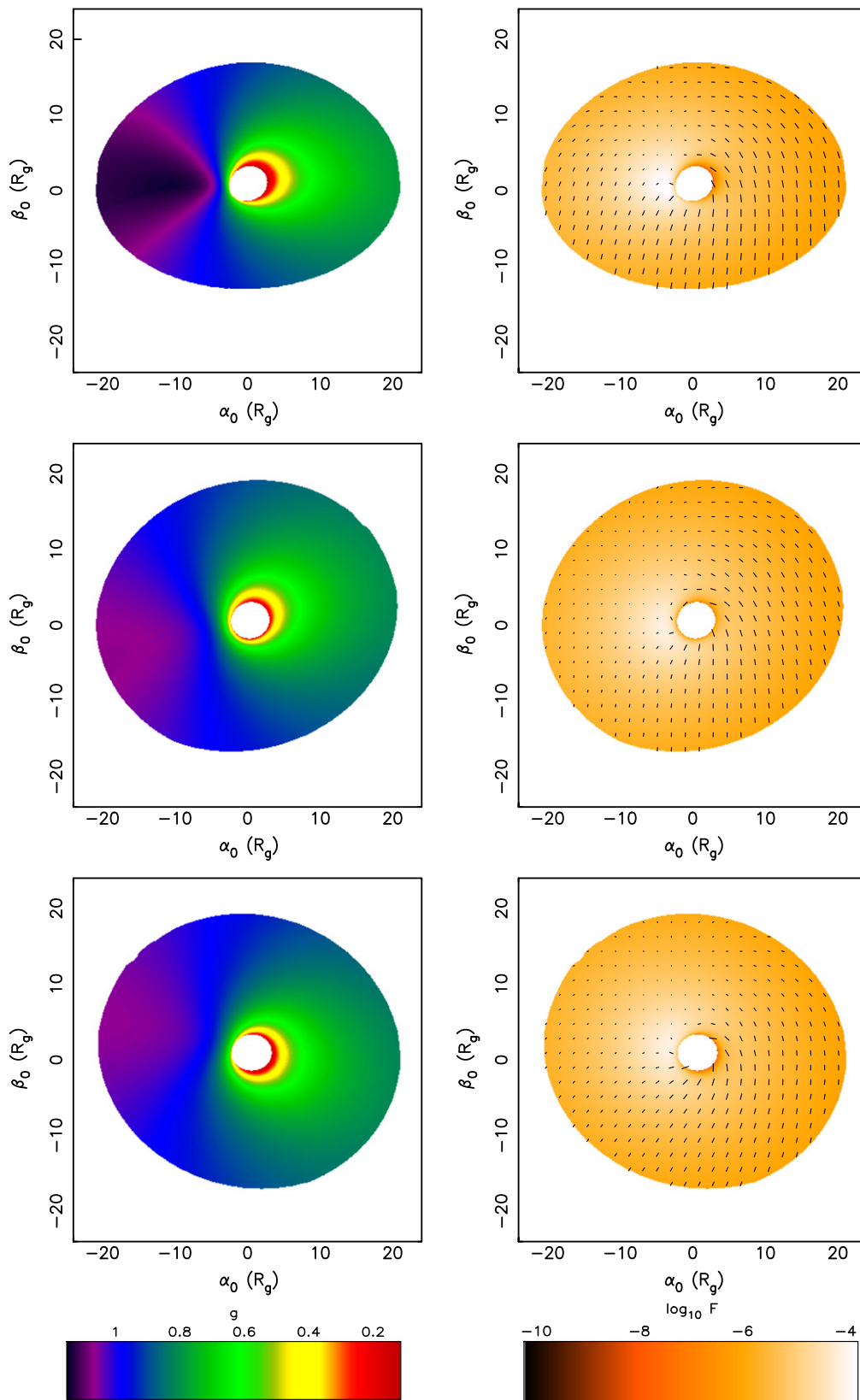
Figure 7. Images of the flow for three precession angles for the model with $i = 30°$, $\Phi = 180°$, $\beta = 10°$, and $h/r = 0.1$. The left side shows blueshift and the right side shows flux with the polarization vector overlaid, normalized to the maximum observed polarization degree. The three precession angles shown, in units of cycles, are $\omega = 0$, 0.3125, and 0.625, from top to bottom, respectively. Full animations corresponding to these images can be found at http://figshare.com/articles/Polarization_modulation_gifs/1351920. Individual animations can alternatively be found on YouTube: www.youtube.com/watch?v=TSe–iXofu8&feature=youtu.be (blueshift) and www.youtube.com/watch?v=GjlIRfkor_s&feature=youtu.be (flux and polarization).
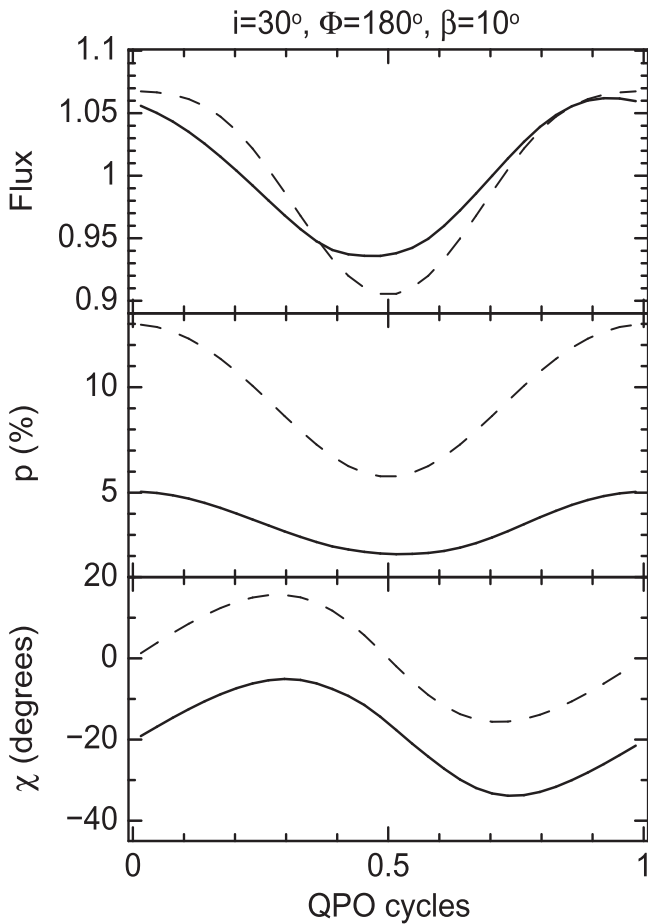
Figure 8. Flux, polarization degree, and polarization angle plotted against QPO phase for the low inclination model. Solid and dashed lines again refer to the fully relativistic model and the Newtonian comparison, respectively. The fractional rms's (for the full model) in the first and second harmonics, respectively, are 4.6% and 0.25% for the flux. The *absolute* rms's in the first and second harmonics are, respectively, 1.1% and 0.05% for the polarization degree and respectively $10°.0$ and $1°.0$ for the polarization angle.

images shown in Figures 5 and 7 can be found at http://figshare.com/articles/Polarization_modulation_gifs/1351920 (additionally, YouTube links for individual movies are given in the figure captions).

Figure 8 shows the flux, polarization degree, and polarization angle plotted against QPO phase for this model, again with the results of the simple Newtonian calculation represented with dashed lines. Here, the flux is less affected by light bending, since the angle between the flow spin axis and the LOS never gets particularly large. GR effects only reduce the mean and rms of the polarization degree and angle, with the phase of the oscillations only slightly modified from the Newtonian approximation. The amplitude of flux variability is lower here than in the high inclination case, although the inclination dependence of the amplitude is far more pronounced for the Newtonian approximation than for the full calculation. This is again attributable to light bending. The absolute rms of the polarization degree is comparable to the high inclination case, but the *fractional* variation in polarization degree is actually significantly larger here than for the high inclination model. This can be understood from Figure 4, which shows that the emergent polarization degree is a far steeper function of μ_e for large μ_e. However, the mean

polarization degree is far lower here than for the high inclination angle, and these two considerations happen to balance. The amplitude of the polarization angle oscillation is greater for the low inclination model, which is a purely geometrical effect. It is clear from Figure 8 that the polarization degree and flux are nearly in phase for this example, in contrast to the results for the high inclination model. We find that p lags F by $20°.3$ for the fundamental and χ lags F by $113°.8$. Since we see no secondary image from the underside of the flow for this viewing angle, assuming the material between the disk and flow to be optically thick does not change our results.

4.2. Parameter Study

We now consider the full range of viewing angles for the specific geometrical setup described at the start of this section. The corresponding parameter exploration in VPI13 considered viewing angles ranging from $0° \leqslant i \leqslant 90°$ and $0° \leqslant \Phi \leqslant 180°$. However, our use of the Kerr metric introduces a subtle asymmetry (which disappears for $a = 0$ of course), meaning that we must explore the range $0° \leqslant \Phi \leqslant 360°$ to be exhaustive. We use a reduced resolution of 80×80 pixels and consider 16 precession angles. When we test for the specific high and low inclination models considered above, we find that this reduced resolution provides a very good approximation to the high resolution run.

In Figure 9, we use colors and contours to plot four different quantities for the entire range of viewing angles. Each plot has its own logarithmic scale. The top-left plot shows the fractional rms amplitude of the flux modulation, $\sigma_F/\langle F \rangle$, for the first harmonic only. The contours in this plot are labeled as percentages and labels always face the uphill direction. We see that the amplitude of the QPO increases with i as we might expect from the previous subsection. This is consistent with observations (Schnittman et al. 2006a; Motta et al. 2015; Heil et al. 2015). We note that this rise of amplitude with inclination angle would be even more pronounced if we had assumed secondary images to be blocked by optically thick material, since these wash out variability for high viewer inclinations. The plot (and all subsequent plots) is nearly symmetric about $\Phi = 180°$, but a subtle asymmetry is introduced by the assumption of high spin. The top-right plot shows the absolute rms amplitude of the polarization degree modulation σ_p, again for the fundamental only, with contours labeled as percentages. This peaks at $i \sim 60°-70°$. The bottom-right plot shows the mean polarization degree $\langle p \rangle$, again with contours labeled as percentages. We see that this increases with i. For small i, the mean polarization degree is very low indeed, which leads to the *fractional* rms amplitude of the polarization degree modulation becoming very large for low inclinations. However, it is likely the *absolute* rms amplitude that is relevant to detection.

The bottom left plot shows the absolute rms variability of polarization angle σ_χ, with contours now labeled in degrees, again for the first harmonic only. Note that the polarization angle is only defined on an interval of $180°$, since upward polarization is indistinguishable from downward polarization. This can produce phase wrapping: e.g., if χ oscillates between a minimum and maximum of $80°$ and $100°$ but is defined on the interval $-90°$ to $90°$, the measured χ will jump from $90°$ to $-90°$ at some point during the QPO cycle, producing a spuriously large rms measurement. To avoid this, for every
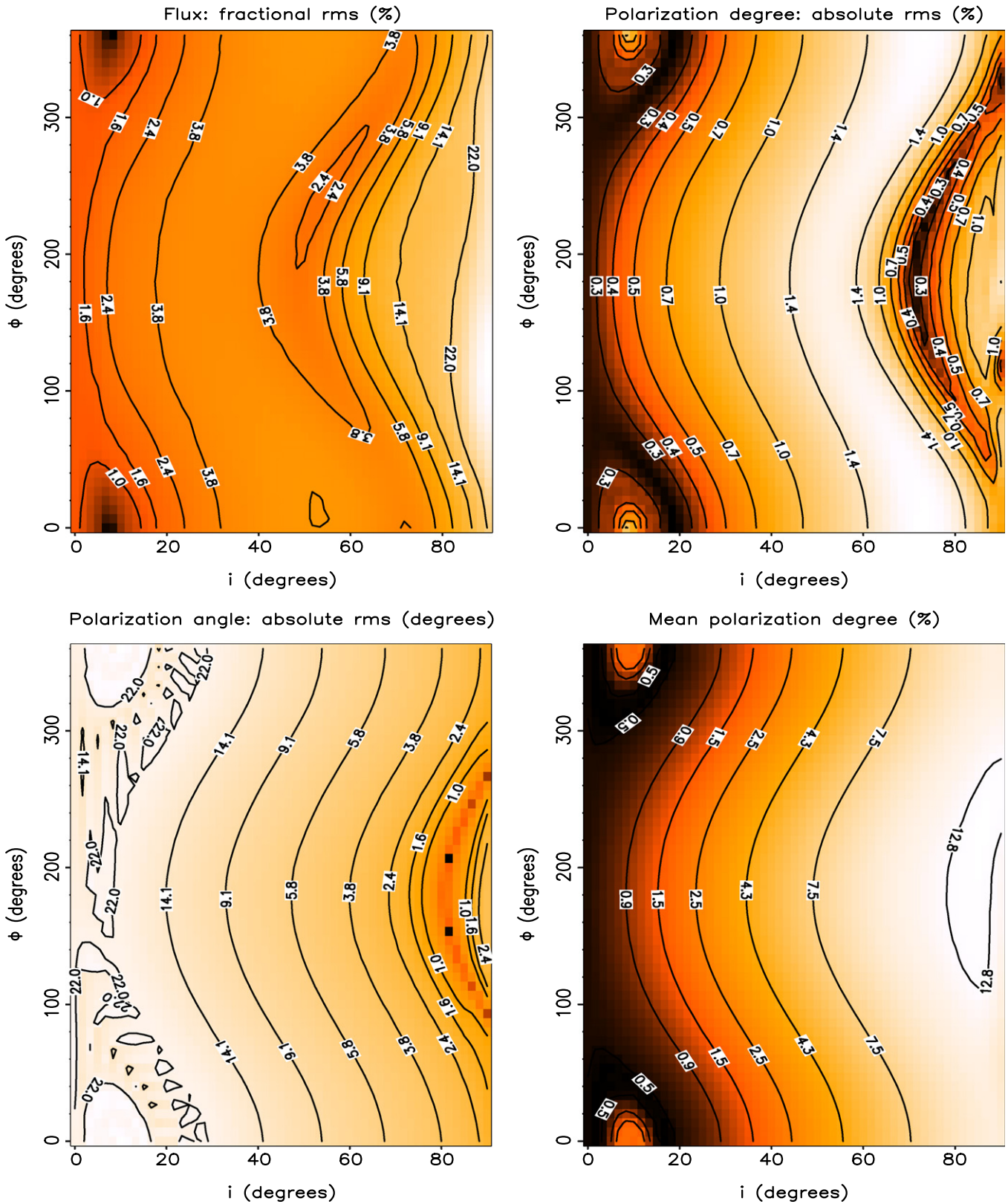
Figure 9. Top left: fractional rms in the first harmonic of the flux modulation plotted as a function of the two viewing angles, i and Φ, with contours labeled as percentages. Top right: absolute rms in the first harmonic of the polarization degree modulation, with contours again labeled as percentages. Bottom right: mean polarization degree, with contours once again labeled as percentages. Bottom left: absolute rms in the first harmonic of the polarization angle modulation, with contours now labeled in degrees. The colors in each plot follow separate logarithmic scales. We see that the amplitude of the flux and polarization degree modulations increase with inclination angle, i, whereas the amplitude of the polarization angle modulation reduces with i. Note the slight asymmetry in all plots around $\Phi = 180°$, which occurs because $a \neq 0$.
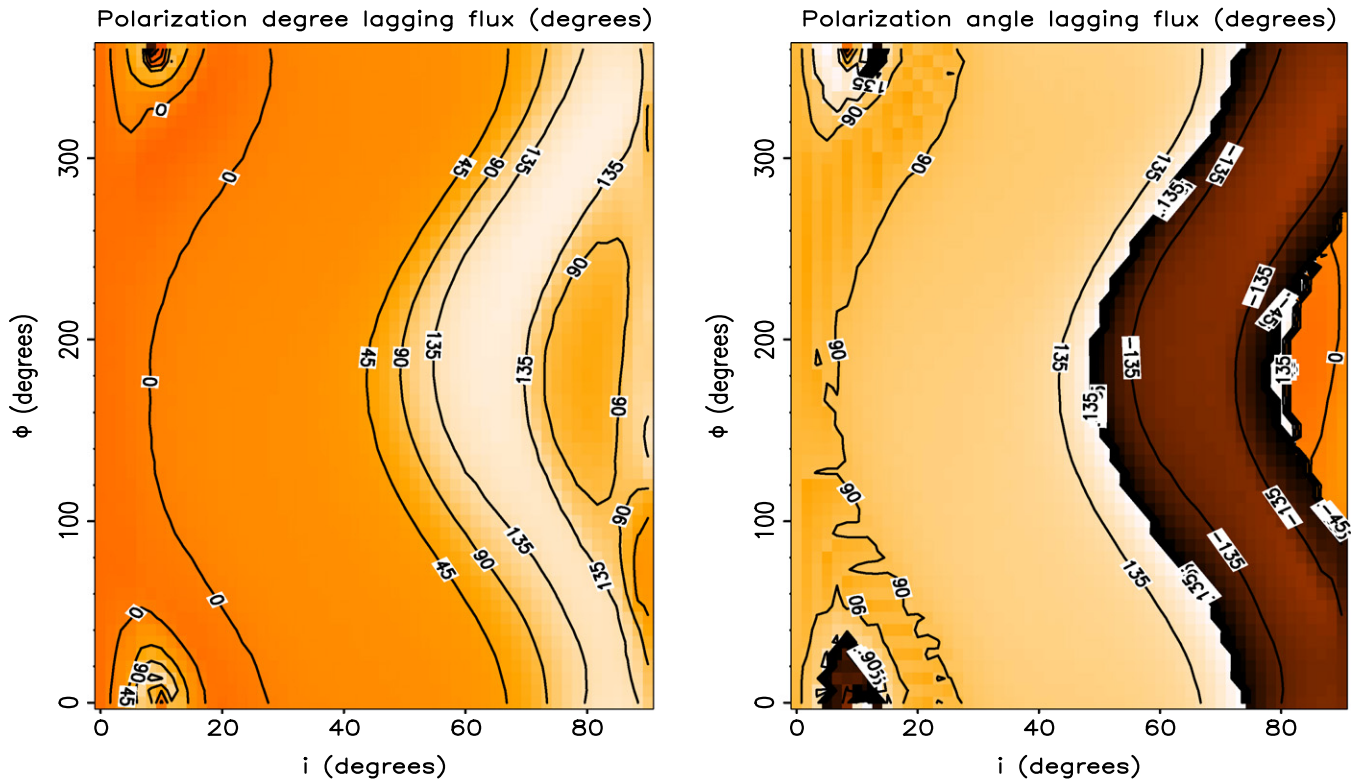
Figure 10. Left: phase lag in degrees between the polarization degree and the flux, with positive lag meaning that p lags F. Here, we only plot the fundamental and color scales linearly from $-180°$ (darkest) to $180°$ (lightest). We see that the model predicts the oscillation in polarization degree to lag the first harmonic of flux for almost the full range of viewing angles. Right: phase lag between polarization angle and flux. The model predicts the magnitude of the phase lag between χ and F to be large for most of the parameter space.

combination of i and Φ, we define χ for the first QPO phase on the interval $-90°$ to $90°$. For each subsequent value of the QPO phase, we first calculate χ on the same interval, but also try adding 0, $180°$, and $-180°$, and choose the interval that minimizes the difference from the previous measurement of χ. We see that the amplitude decreases with inclination angle, but is above $1°$ for most of the parameter space.

In Figure 10 (left), we plot the phase lag between polarization degree and flux against i and Φ. Here, positive lags mean that p lags F and we again consider only the fundamental. We see that p lags F for nearly all viewing angles. In the right panel, we instead plot the phase lag between χ and F. Here we see phase wrapping at $i \sim 60°$, which occurs because the lag between the two functions is only defined on the interval $-180°$ to $180°$. The magnitude of the lag is large for most of the parameter space. This can be understood by looking at the images in Figures 5 and 7. The peak in χ for our coordinate system occurs approximately when we see the flow spin axis tilted the farthest to the left. The flux rarely peaks close to this phase in the precession cycle. If a high enough signal to noise ratio can be achieved to observe these lags, they may provide a powerful extra diagnostic.

5. DISCUSSION

We have calculated the polarization signature predicted by the precessing inner flow model for low frequency QPOs. We find that the polarization degree and angle are expected to be modulated on the QPO period.

5.1. Assumptions

In our analysis, we calculate the GR effects very accurately but make a number of simplifying assumptions about the properties of the inner accretion flow. We use analytical parameterizations for the angular dependence of intensity and polarization degree of radiation emerging from the flow. Since these parameterizations are based on the calculations of ST85, this is a reasonable assumption but there is scope to extend this work in the future. Our parameterization is only valid for one value of optical depth ($\tau = 1$) and so we cannot explore the dependence of our results on this parameter. In addition, we assume that the angular dependence of the flow emissivity can be separated from the radial and energy dependencies (Equation (9)). In reality, it is likely that the shape of the emitted spectrum depends on both radius *and* viewing angle. Since the outer part of the flow is illuminated by a greater flux of cool disk photons, the spectrum should be softer for larger r, giving rise to the observed time lags (Kotov et al. 2001; Ingram & van der Klis 2013). There is now observational evidence that the spectral shape of the flow depends on viewing angle (Heil et al. 2015; Ingram & van der Klis 2015). Similarly, the angular dependence of polarization degree will likely depend on the energy of the emitted photon, and also perhaps the radius it was emitted from. We also expect the flow optical depth, and therefore the mean polarization degree, to depend on the truncation radius/spectral state. For a low luminosity hard state we expect τ to drop below unity and polarization degree to reach $\sim 50\%$ (see Viironen & Poutanen 2004). Replacing our simple parameterization with a full Monte Carlo simulation in the future will be a significant improvement upon this work.

We also effectively assume that the seed photon luminosity stays constant during a QPO cycle. This is a good assumption if the seed photon luminosity is completely dominated by internally generated photons (Veledina et al. 2011a; VPI13). However, the luminosity of disk photons incident on the flow will vary as the misalignment between the disk and flow changes over the course of a precession cycle. A calculation of the disk seed photon luminosity as a function of precession angle has yet to be performed taking GR effects fully into account. The relative importance of internally generated seed photons will increase with truncation radius. It should be possible to put constraints on such an evolution of the seed photon origin with X-ray polarimetry, since the polarization degree depends strongly on the scattering order for disk seed photons (see Figure 2 in Viironen & Poutanen 2004).

5.2. Detection

It may be possible to detect the predicted polarization degree and angle modulation in the near future with a dedicated polarization satellite mission. Here we present a simple calculation to roughly assess detectability. X-ray polarimeters generally use either Thomson scattering (e.g., the *Polarization Spectroscopic Telescope Array*; *PolSTAR*) or the photoelectric effect (e.g., *Gravity & Extreme Magnetism SMEX; GEMS*). Scattering polarimeters measure the landing position of scattered photons, which travel preferentially in the direction perpendicular to their electric field vector (e.g., Guo et al. 2013). Photoelectric effect polarimeters track the direction of photoelectrons, which are preferentially emitted in the direction parallel to the incoming electric field vector (e.g., Black et al. 2010). In either case, an estimate for the polarization angle of each incident photon, χ_k (i.e., for the kth photon), can be recorded. When many photons are incident on the detector, a polarized signal will exhibit a sinusoidal modulation with a distribution (Lei et al. 1997; Krawczynski et al. 2011; Kislat et al. 2014):

$$f\left(\chi_k\right) \propto 1 + p\,\mu\,\cos\!\left[2\left(\chi_k - \chi\right)\right], \qquad (30)$$

where χ is the "true" polarization angle of the source, p is the "true" polarization degree, and μ is the modulation factor. The performance of a polarimeter can be characterized by the modulation factor, since it governs the distribution of a 100% polarized signal. When C photons are incident on the detector, the measurement error on p is (Kislat et al. 2014)

$$dp \approx \sqrt{\frac{2/\mu^2 - p^2}{C - 1}}, \qquad (31)$$

when C is sufficiently large to be in a Gaussian regime (note, p is represented here as a fraction rather than a percentage). The measurement error on χ (in radians) is

$$d\chi \approx \frac{1}{p\mu\sqrt{2(C - 1)}}. \qquad (32)$$

Detection of a ∼1 s QPO requires a time resolution ≲0.1 s. Very few photons can likely be collected in such a short time and therefore a high time resolution time series of individual Stokes parameters would indeed be very noisy. However, it is possible to stack into QPO phase bins (Tomsick & Kaaret 2001), resulting in one folded time series. If we stack into N phase bins, the number of counts detected per phase bin

is simply $C = R\,T/N$, where R is the mean count rate and T is the total exposure time. We can estimate that detection of a QPO in the polarization degree requires a measurement error in each phase bin around one-fifth of the absolute rms variability amplitude, $dp \sim \sigma_p/5$. Thus, the mean count rate we must be able to detect for the observation is

$$R \sim \frac{25N}{T\sigma_p^2}\left[\frac{2}{\mu^2} - \langle p\rangle^2\right]. \qquad (33)$$

We can estimate the count rate required to detect a modulation in polarization angle in a similar manner. In this case

$$R \sim 4.1 \times 10^4 \frac{N}{T\left\langle p\right\rangle^2 \mu^2\sigma_\chi^2}, \qquad (34)$$

where σ_χ is in degrees. In Figure 11, we show these required count rates for all of the parameter space assuming $N = 8$ phase bins, an exposure of $T = 200$ ks, and a modulation factor of $\mu = 0.5$. The plots on the left and right are for polarization degree and angle, respectively. We see that to detect either modulation at all, a polarimeter must have the sensitivity to measure a count rate above 40 c/s, and a count rate of ∼60 c/s opens up a reasonably large fraction of parameter space ($i \sim 40°$–$75°$) in which both modulations can be detected. The same folding method can be used to measure lags between the polarization properties and the flux, although this may require a more challenging sensitivity.

A number of missions that have been proposed for *NASA*'s Small Explorer Program (SMEX) should be able to detect count rates ≳40 c/s. *PolSTAR* (the satellite incarnation of the balloon experiment *X-Calibur*; Guo et al. 2013) is sensitive to the ∼10–20 keV energy range in which the Comptonized spectrum dominates, and would therefore be ideal for this application. The soft X-ray missions *GEMS* (Black et al. 2010) and the *Imaging X-ray Polarimetry Explorer* (Weisskopf et al. 2008) should also be able to measure a similar count rate; however, contribution to the flux from the constant disk component at softer energies will dilute the variability amplitude of the polarization signature, making detection more challenging (rms ≈ rms$_{\text{flow}}[1 - x_{\text{disk}}]$, where x_{disk} is the fraction of the flux contributed by the disk). Disk dilution is not a problem in the hard state, but here the flux is lower and the QPOs are generally not as coherent as in the HIMS.

5.3. Implications

The detection of a polarization modulation on the QPO frequency would have strong implications. First, this would confirm that the QPO is indeed a geometric effect, as is strongly hinted in the literature at the moment (Motta et al. 2015; Heil et al. 2015; Ingram & van der Klis 2015). It will also provide a strong test for the Lense–Thirring QPO model. This is fairly profound in itself, since Lense–Thirring precession has never been unambiguously observed in the strong field regime, but this also has implications with regard to making spin measurements. Current spin measurements from disk spectral fitting (e.g., Kolehmainen & Done 2010; Steiner et al. 2011) assume that the BH and binary spin axes are aligned, in contradiction of the Lense–Thirring QPO model. Careful modeling of QPO properties can be used to estimate the
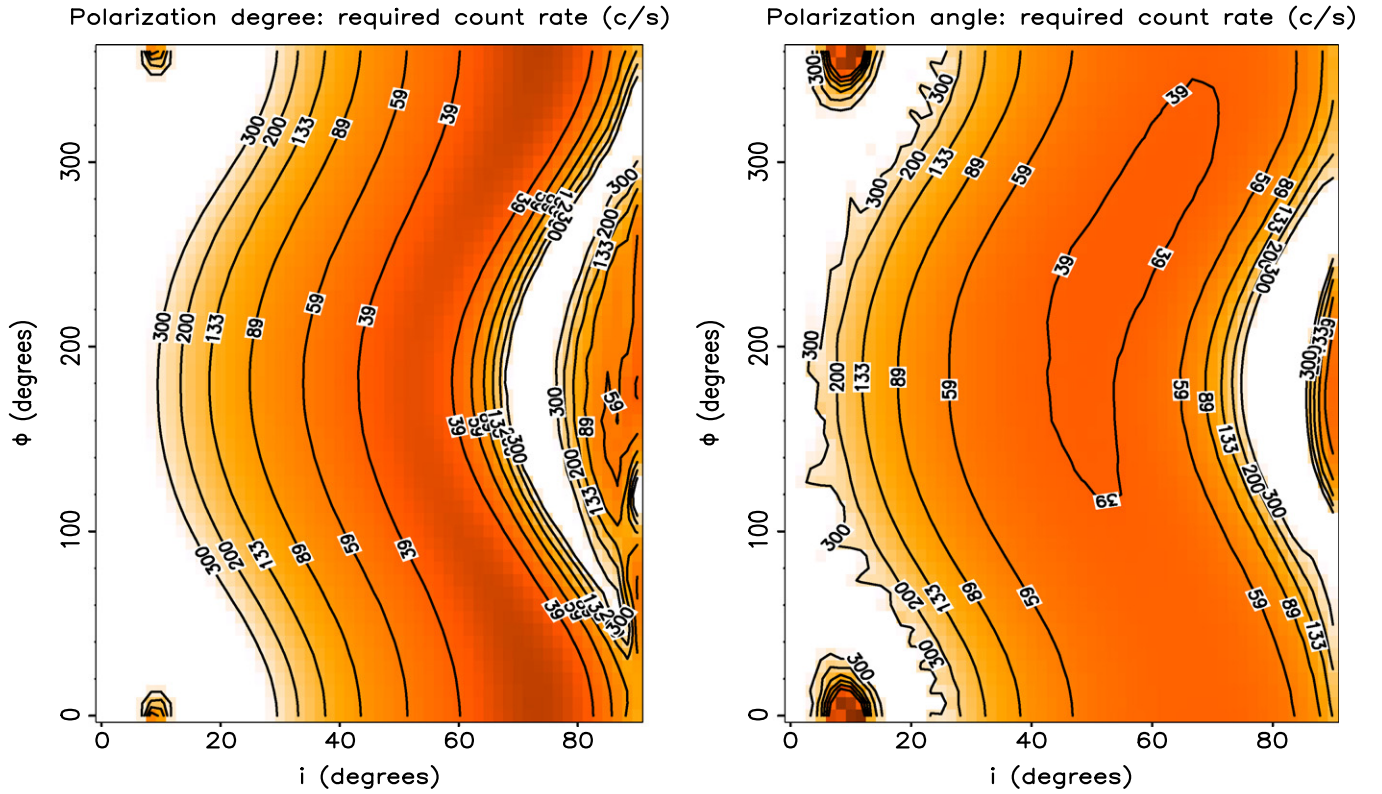
Figure 11. Required count rate in order to detect a modulation in polarization degree (left) and angle (right). We assume a 200 ks exposure and a modulation factor of $\mu = 0.5$. See the text for more details.

misalignment angle β to improve the spectroscopic measurements and also the very measurement of the QPO frequency itself gives an orthogonal spin estimate if high frequency QPOs are also present (Ingram & Motta 2014; Motta et al. 2014).

6. CONCLUSIONS

We find that the polarization signature emitted from a truncated disk/precessing inner flow geometry oscillates on the QPO frequency. The modulation in polarization degree has an absolute rms that increases gradually with viewer inclination angle, peaking at 1.5% for $i \sim 60°$. In contrast, the absolute rms of the polarization angle modulation is higher for lower inclination angles. For the polarization degree, this inclination dependence is mainly due to the assumed angular dependence of the polarization degree and emissivity for Compton scattering, which we parameterize to agree with the calculations of ST85. Although our parameterization is only appropriate for an optical depth of $\tau = 1$, we note that the results of ST85 are qualitatively similar for optical depths up to $\tau \sim 2.5$. The inclination dependence of the polarization angle mainly depends on the precessing geometry and GR effects, so it is robust to our assumptions about the Compton scattering process. Our calculations here only consider one specific flow geometry, and we explore the full range of viewing angles. In the future, we will also explore the effects of changing parameters such as the truncation radius and spin. In particular, we note that assuming a larger misalignment angle, β, will increase the predicted amplitudes of all modulations.

We find through a rough calculation that, in order to detect this effect for a reasonable fraction of parameter space, an X-ray polarimeter will need to detect a $10-20$ keV count rate of $\gtrsim 60$ c/s from a bright object displaying QPOs. The current

generation of proposed X-ray polarimetry missions will likely fill this requirement. In particular, NASA's *PolSTAR* is suited to this application due to its sensitivity to hard X-rays.

APPENDIX A
THE KERR SPACE TIME

The non-zero entries of the Kerr metric can be expressed in Boyer–Lindquist coordinates as

$$g_{tt} = -\left(1 - \frac{2r}{\Sigma}\right), \quad g_{t\phi} = \frac{-2ar\sin^2\theta}{\Sigma},$$

$$g_{\phi t} = g_{t\phi}, \quad g_{rr} = \frac{\Sigma}{\Delta},$$

$$g_{\theta\theta} = \Sigma, \quad g_{\phi\phi} = \frac{\mathcal{A}\sin^2\theta}{\Sigma}, \tag{35}$$

where $\Sigma \equiv r^2 + a^2\cos^2\theta$, $\Delta \equiv r^2 - 2r + a^2$, and $\mathcal{A} \equiv (r^2 + a^2)^2 - \Delta a^2\sin^2\theta$. The four-momentum of photons traveling in the Kerr space time can be expressed as (Carter 1968; Misner et al. 1973; Dovciak 2004)

$$p^t = \Sigma^{-1}\left[a\left(l - a\sin^2\theta\right) + \left(r^2 + a^2\right)\left(r^2 + a^2 - al\right)/\Delta\right] \tag{36}$$

$$p^r = R_{sgn} \Sigma^{-1} \left[\left(r^2 + a^2 - al \right)^2 - \Delta \left[(l - a)^2 + q^2 \right] \right]^{1/2}$$
(37)

$$p^\theta = -\Theta_{sgn} \Sigma^{-1} \left[q^2 - \cot^2 \theta \left(l^2 - a^2 \sin^2 \theta \right) \right]^{1/2}$$
(38)

$$p^\phi = \Sigma^{-1} \left[l / \sin^2 \theta - a + a \left(r^2 + a^2 - al \right) / \Delta \right],$$
(39)

where Carter's constants of motion, l , and q^2 are given in the main text and the sign of the radial and polar coordinates is denoted by R_{sgn} and Θ_{sgn}. Both of these are positive for the case of an even number of turning points between the viewer and the emission point and negative for an odd number.

APPENDIX B
THE FLOW NORMAL

According to the equivalence principle, we can always define a "free-falling laboratory" frame in which GR reduces to Special Relativity. Mathematically, this can be achieved by defining a tetrad of orthonormal unit four-vectors. We require the flow normal n^μ to be part of such an orthonormal tetrad in order to calculate the emission angle from it. We calculate the r, θ, and ϕ components of n^μ by transforming $\hat{z}_f$ into Boyer–Lindquist coordinates (see Appendix C). The time-like unit vector in the tetrad is simply u^μ, i.e., the instantaneous rest frame (e.g., Krawczynski 2012; Wilkins & Fabian 2012). The time-like component of n^μ can thus be calculated by setting $n^\mu u_\mu = 0$ to give

$$n^t = -\frac{\hat{z}_f^d g_{d\nu} u^\nu}{g_{t\mu} u^\mu},$$
(40)

where $d = r$, θ, ϕ but Greek letters run from t to ϕ as usual. Finally, we normalize to ensure $n^\mu n_\mu = 1$.

APPENDIX C
COORDINATE TRANSFORMS

We can convert from the BH angles θ and ϕ to the flow angles θ_f and ϕ_f using the formulae

$$\cos \theta_f = \hat{r} \cdot \hat{z}_f$$
(41)

and

$$\tan \phi_f = \frac{\hat{r} \cdot \hat{y}_f}{\hat{r} \cdot \hat{x}_f}.$$
(42)

This gives

$$\cos \theta_f = \sin \theta \sin \beta \cos(\omega - \omega_0 - \phi) + \cos \theta \cos \beta$$
(43)

and

$$\tan \phi_f = \frac{\sin \theta \sin(\omega - \omega_0 - \phi)}{\cos \theta \sin \beta - \sin \theta \cos \beta \cos(\omega - \omega_0 - \phi)}.$$
(44)

The reciprocal conversion is

$$\cos \theta = \cos \theta_f \cos \beta + \sin \theta_f \cos \phi_f \sin \beta$$
(45)

and

$$\tan \phi = \frac{\begin{aligned} -\sin \theta_f \big[\cos \beta \sin(\omega - \omega_0) \cos \phi_f \\ + \cos(\omega - \omega_0) \sin \phi_f \big] \\ + \cos \theta_f \sin \beta \sin(\omega - \omega_0) \end{aligned}}{\begin{aligned} \sin \theta_f \big[-\cos \beta \cos(\omega - \omega_0) \cos \phi_f \\ + \sin(\omega - \omega_0) \sin \phi_f \big] \\ + \cos \theta_f \sin \beta \cos(\omega - \omega_0). \end{aligned}}$$
(46)

Additionally, since $\hat{z}_b = \hat{z}_f(\omega = \pi)$, we can convert to and from binary angles using the above formulae by setting $\omega = \pi$ (i.e., replacing subscript f with subscript b and replacing ω with π).

Our calculation also requires the conversion of Cartesian coordinates to Boyer–Lindquist coordinates. The two are related as

$$\begin{aligned} x &= \sqrt{r^2 + a^2} \sin \theta \cos \phi \\ y &= \sqrt{r^2 + a^2} \sin \theta \sin \phi \\ z &= r \cos \theta. \end{aligned}$$
(47)

To convert the coordinates of a three-vector, A, from a Cartesian to a Boyer–Lindquist representation, we simply apply the general formula

$$A^{b'} = \frac{\partial x^{b'}}{\partial x^a} A^a,$$
(48)

where b' can take the values r, θ, and ϕ and a can take the values x, y, and z. Combining Equation (47) gives

$$r^2 = \frac{1}{2} \left[\rho^2 - a^2 + \sqrt{\left(\rho^2 - a^2 \right)^2 + 4a^2 z^2} \right],$$
(49)

where $\rho^2 \equiv x^2 + y^2 + z^2$, along with the familiar expressions $\cos \theta = z/r$ and $\tan \phi = y/x$. The differentials of r can be expressed as

$$\begin{aligned} \frac{\partial r}{\partial x} &= \sqrt{1 + \left(\frac{a}{r} \right)^2} \frac{\sin \theta \cos \phi}{2} \left[1 + \frac{r^2 - a^2 \cos^2 \theta}{\Sigma} \right] \\ \frac{\partial r}{\partial y} &= \sqrt{1 + \left(\frac{a}{r} \right)^2} \frac{\sin \theta \sin \phi}{2} \left[1 + \frac{r^2 - a^2 \cos^2 \theta}{\Sigma} \right] \\ \frac{\partial r}{\partial z} &= \frac{\cos \theta}{2} \left[1 + \frac{r^2 + a^2 \left(1 + \sin^2 \theta \right)}{\Sigma} \right]. \end{aligned}$$
(50)

and for θ:

$$\begin{aligned} \frac{\partial \theta}{\partial x} &= \sqrt{1 + \left(\frac{a}{r} \right)^2} \frac{\cos \theta \cos \phi}{2r} \left[1 + \frac{r^2 - a^2 \cos^2 \theta}{\Sigma} \right] \\ \frac{\partial \theta}{\partial y} &= \sqrt{1 + \left(\frac{a}{r} \right)^2} \frac{\cos \theta \sin \phi}{2r} \left[1 + \frac{r^2 - a^2 \cos^2 \theta}{\Sigma} \right] \\ \frac{\partial \theta}{\partial z} &= -\frac{r \sin \theta}{\Sigma}. \end{aligned}$$
(51)

Note that these expressions, as expected, reduce to the relations for spherical polar coordinates in the Schwarzschild limit. The case of $\sin\theta = 0$ must be treated separately, although this is rather straightforward. The differentials of ϕ are the same as the case of spherical polars. These can then be substituted into Equation (48) in order to convert the vector. The reciprocal conversion, from Boyer–Lindquist to Cartesian, is far simpler, requiring the differentials of Equations (47) with respect to the Boyer–Lindquist coordinates.

REFERENCES

Altamirano, D., Ingram, A., van der Klis, M., et al. 2012, ApJL, 759, L20
Axelsson, M., Hjalmarsdotter, L., & Done, C. 2013, MNRAS, 431, 1987
Belloni, T. M. 2010, Lecture Notes in Physics, Vol. 794 (Berlin: Springer)
Black, J. K., Deines-Jones, P., Hill, J. E., et al. 2010, Proc. SPIE, 7732, 77320
Cabanac, C., Henri, G., Petrucci, P.-O., et al. 2010, MNRAS, 404, 738
Carter, B. 1968, PhRv, 174, 1559
Chandrasekhar, S. 1960, Radiative Transfer (New York: Dover)
Dexter, J., & Agol, E. 2009, ApJ, 696, 1616
Dexter, J., & Fragile, P. C. 2011, ApJ, 730, 36
Done, C., Gierlinski, M., & Kubota, A. 2007, A&A, 15, 1
Dovciak, M. 2004, PhD thesis, Charles University in Prague
Dovčiak, M. 2010, in X-ray Polarimetry: A New Window in Astrophysics, ed. R. Bellazzini et al. (Cambridge: Cambridge Univ. Press), 95
Dovčiak, M., Karas, V., Matt, G., & Goosmann, R. W. 2008a, MNRAS, 384, 361
Dovčiak, M., Muleri, F., Goosmann, R. W., Karas, V., & Matt, G. 2008b, MNRAS, 391, 32
Esin, A. A., McClintock, J. E., & Narayan, R. 1997, ApJ, 489, 865
Ferguson, D. C. 1973, ApJ, 183, 977
Ferguson, D. C. 1976, ApJ, 205, 247
Fragile, P. C. 2009, ApJL, 706, L246
Fragile, P. C., Blaes, O. M., Anninos, P., & Salmonson, J. D. 2007, ApJ, 668, 417
Fragile, P. C., & Meier, D. L. 2009, ApJ, 693, 771
Frank, J., King, A., & Raine, D. J. 2002, Accretion Power in Astrophysics (3rd ed.; Cambridge: Cambridge Univ. Press)
Ghisellini, G., Guilbert, P. W., & Svensson, R. 1988, ApJL, 334, L5
Gilfanov, M. 2010, The Jet Paradigm, (Vol. 749; Berlin Springer)
Guo, Q., Beilicke, M., Garson, A., et al. 2013, APh, 41, 63
Heil, L. M., Uttley, P., & Klein-Wolt, M. 2015, MNRAS, 448, 3348
Ichimaru, S. 1977, ApJ, 214, 840
Ingram, A., & Done, C. 2010, MNRAS, 405, 2447
Ingram, A., & Done, C. 2011, MNRAS, 415, 2323
Ingram, A., & Done, C. 2012a, MNRAS, 419, 2369
Ingram, A., & Done, C. 2012b, MNRAS, 427, 934
Ingram, A., Done, C., & Fragile, P. C. 2009, MNRAS, 397, L101
Ingram, A., & Motta, S. 2014, MNRAS, 444, 2065
Ingram, A., & van der Klis, M. 2015, MNRAS, 446, 3516
Ingram, A., & van der Klis, M. v. d. 2013, MNRAS, 434, 1476
Jaroszynski, M., Abramowicz, M. A., & Paczynski, B. 1980, AcA, 30, 1
Kerr, R. P. 1963, PhRvL, 11, 237
Kislat, F., Clark, B., Beilicke, M., & Krawczynski, H. 2014, arXiv:1409.6214
Kolehmainen, M., & Done, C. 2010, MNRAS, 406, 2206
Kotov, O., Churazov, E., & Gilfanov, M. 2001, MNRAS, 327, 799
Krawczynski, H. 2012, ApJ, 754, 133
Krawczynski, H., Garson, A., Guo, Q., et al. 2011, APh, 34, 550
Lei, F., Dean, A. J., & Hills, G. L. 1997, SSRv, 82, 309
Lense, J., & Thirring, H. 1918, PhyZ, 19, 156
Li, L.-X., Narayan, R., & McClintock, J. E. 2009, ApJ, 691, 847
Loskutov, V. M., & Sobolev, V. V. 1982, Ap, 18, 51
Luminet, J.-P. 1979, A&A, 75, 228
Marin, F., & Dovčiak, M. 2015, A&A, 573, A60
Markwardt, C. B., Swank, J. H., & Taam, R. E. 1999, ApJL, 513, L37
Middleton, M. J., & Ingram, A. R. 2015, MNRAS, 446, 1312
Misner, C. W., Thorne, K. S., & Wheeler, J. A. 1973, Gravitation (San Francisco: Freeman)
Motta, S. E., Belloni, T. M., Stella, L., Muñoz-Darias, T., & Fender, R. 2014, MNRAS, 437, 2554
Motta, S. E., Casella, P., Henze, M., et al. 2015, MNRAS, 447, 2059
Muno, M. P., Morgan, E. H., & Remillard, R. A. 1999, ApJ, 527, 321
Novikov, I. D., & Thorne, K. S. 1973, in Black Holes (Les Astres Occlus), ed. C. Dewitt & B. S. Dewitt
Orosz, J. A., McClintock, J. E., Remillard, R. A., & Corbel, S. 2004, ApJ, 616, 376
Orosz, J. A., Steiner, J. F., McClintock, J. E., et al. 2011, ApJ, 730, 75
Poutanen, J., Krolik, J. H., & Ryde, F. 1997, MNRAS, 292, L21
Poutanen, J., & Svensson, R. 1996, ApJ, 470, 249
Poutanen, J., & Vurm, I. 2009, ApJL, 690, L97
Rapisarda, S., Ingram, A., & van der Klis, M. 2014, MNRAS, 440, 2882
Revnivtsev, M., Gilfanov, M., & Churazov, E. 2001, A&A, 380, 520
Rybicki, G. B., & Bromley, B. C. 1997, e-print (arXiv:astro-ph/9711104)
Rybicki, G. B., & Lightman, A. P. 1979, Radiative Processes in Astrophysics, (Vol. 1979; New York: Wiley-Interscience)
Schnittman, J. D., Homan, J., & Miller, J. M. 2006a, ApJ, 642, 420
Schnittman, J. D., & Krolik, J. H. 2009, ApJ, 701, 1175
Schnittman, J. D., & Krolik, J. H. 2010, ApJ, 712, 908
Schnittman, J. D., Krolik, J. H., & Hawley, J. F. 2006b, ApJ, 651, 1031
Shakura, N. I., & Sunyaev, R. A. 1973, A&A, 24, 337
Sobczak, G. J., McClintock, J. E., Remillard, R. A., et al. 2000, ApJ, 531, 537
Sobolewska, M. A., & Życki, P. T. 2006, MNRAS, 370, 405
Stark, R. F., & Connors, P. A. 1977, Natur, 266, 429
Steiner, J. F., Reis, R. C., McClintock, J. E., et al. 2011, MNRAS, 416, 941
Stella, L., & Vietri, M. 1998, ApJL, 492, L59
Sunyaev, R. A., & Titarchuk, L. G. 1985, A&A, 143, 374
Sunyaev, R. A., & Truemper, J. 1979, Natur, 279, 506
Tagger, M., & Pellat, R. 1999, A&A, 349, 1003
Tananbaum, H., Gursky, H., Kellogg, E., Giacconi, R., & Jones, C. 1972, ApJL, 177, L5
Thorne, K. S., & Price, R. H. 1975, ApJL, 195, L101
Tomsick, J. A., & Kaaret, P. 2001, ApJ, 548, 401
van der Klis, M. 2006, AdSpR, 38, 2675
Veledina, A., & Poutanen, J. 2015, MNRAS, 448, 939
Veledina, A., Poutanen, J., & Ingram, A. 2013, ApJ, 778, 165
Veledina, A., Poutanen, J., & Vurm, I. 2011a, ApJL, 737, L17
Veledina, A., Vurm, I., & Poutanen, J. 2011b, MNRAS, 414, 3330
Viironen, K., & Poutanen, J. 2004, A&A, 426, 985
Wagoner, R. V., Silbergleit, A. S., & Ortega-Rodríguez, M. 2001, ApJL, 559, L25
Weisskopf, M. C., Bellazzini, R., Costa, E., et al. 2008, in Proc. SPIE, 7011, 70111
Wilkins, D. R., & Fabian, A. C. 2012, MNRAS, 424, 1284
Yan, S.-P., Ding, G.-Q., Wang, N., Qu, J.-L., & Song, L.-M. 2013, MNRAS, 434, 59
Zamaninasab, M., Eckart, A., Dovčiak, M., et al. 2011, MNRAS, 413, 322